nature physics

Article

https://doi.org/10.1038/s41567-024-02457-5

Emergence of large-scale mechanical spiral waves in bacterial living matter

Received: 1 June 2023

Accepted: 27 February 2024

Published online: 04 April 2024

Check for updates

Shiqi Liu, Ye Li, Yuhao Wang & Yilin Wu

Propagating spiral waves have been discovered in various chemical, biological and physical systems. Spiral waves in multicellular organisms are often associated with essential living functions. Although certain eukaryotic microorganisms have long been known to generate spiral waves, evidence of spiral wave pattern has been lacking in the bacterial world. Here we report the discovery of a unique form of propagating spiral waves in dense bacterial populations where cells engage in cyclic force-generating processes driven by a grappling-hook-like motile organelle called type-IV pilus motor. Specifically, we discovered that synchronization of pilus activity in the bacterial living matter leads to large-scale spatiotemporal regulation of tension force in the form of propagating spiral waves. Theoretical modelling reveals that the spiral tension waves result from non-reciprocity in cell–cell interactions. Our findings reveal a mechanism of large-scale force regulation in bacterial world and may shed light on the emergent mechanics of biofilms and microbiomes. Pilus-driven bacterial living matter also provides a mechanical active medium for studying electrical or chemical spiral waves in living systems.

Propagating waves with spiral patterns are discovered in various chemical, biological and physical systems[1–3] such as chemical excitable medium[4–6], cardiac tissue[7] and neural networks[8]. The onset of spiral waves in multicellular organisms is often associated with essential living functions[8,9]. For example, spiral waves of electrochemical activities in neural tissues serve as a rhythmic organizer in cortex neurons[8], while those in cardiac tissues may cause ventricular arrhythmia[7,10]. Although certain eukaryotic microorganisms have long been known to generate spiral waves[11,12], spiral wave patterns have not been observed in the bacterial world. Here we report the discovery of a unique form of propagating spiral waves in dense bacterial populations where cells engage in cyclic force-generating processes driven by type IV pili. Type IV pilus is a motile organelle shared by diverse bacterial species[13,14]; working like grappling hooks, it is the most powerful molecular motor known to date[15]. We discovered that synchronization of pilus activity in the bacterial living matter leads to large-scale spatiotemporal regulation of mechanical forces in the form of propagating spiral tension waves. The spiral tension wave is highly stable with stationary cores, resembling those seen in the electrical activity of heart tissues during ventricular arrhythmia[7,10]. Theoretical modelling suggests that the striking pattern of spiral tension waves is a result of non-reciprocal coupling between pilus activities. As type IV pili are widespread in bacteria, our findings may shed light on the emergent mechanics of biofilms[16] and microbiomes in natural and clinical settings. Moreover, the unique wave pattern provides a tractable mechanical analogue for studying electrical or chemical spiral waves in diverse living systems[7,10,17,18].

Emergence of spiral waves in bacterial living matter

Powered by an adenosine triphosphate (ATP)-driven translational molecular motor[13,14], type IV pilus extends and retracts in a cyclic manner[19–22], generating pulling forces up to ~100 pN (ref. 15). Using naturally developed surface colonies of the model organism *Pseudomonas aeruginosa*[14], we discovered the presence of propagating spiral waves in the colonies of this species. The waves appeared in the form of ordered light-intensity oscillation in the phase-contrast images of the colonies over a macroscopic length scale much greater than the cell size (~2–4 μm in length and 0.8 μm in width) (Fig. 1a,b and Supplementary Video 1). The period and the wavefront propagating speed of such spiral waves ranged from ~3–10 min and ~1–3 μm s^{-1}, respectively. Type-IV

Department of Physics and Shenzhen Research Institute, The Chinese University of Hong Kong, Shatin, NT, P.R. China. e-mail: ylwu@cuhk.edu.hk

https://doi.org/10.1038/s41567-024-02457-5

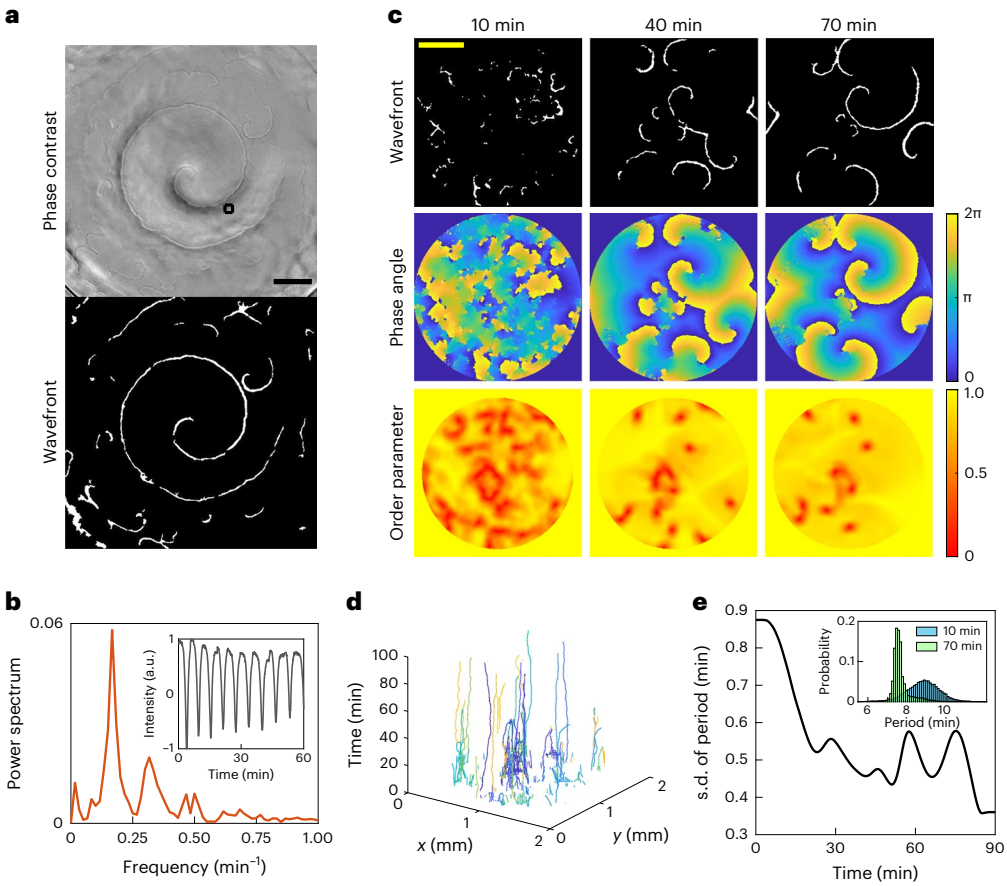

Fig. 1 | Self-organization of propagating spiral waves with stationary cores in quasi-two-dimensional bacterial living matter. a, Spiral wave pattern in a piliated *P. aeruginosa* (PA14 *flgK*::Tn5) colony. Wavefronts of the propagating spiral waves are visible in background-corrected phase-contrast images (upper) and can be traced based on the variation of light intensity in a sequence of phase-contrast images (lower) (Methods). Scale bar, 500 μm. Also see Supplementary Video 1 for the original phase-contrast images. **b**, Fourier-transformed power spectrum of the temporal variation of phase-contrast image intensity (inset) inside the black box specified in **a** (100.8 μm × 100.8 μm) (Methods). The power spectrum for this representative case shows a prominent first-order peak at 0.17 min^{-1}. **c**, Development of propagating spiral waves in artificial bacterial films of *P. aeruginosa*. Upper row, traces of wavefronts (Methods). Middle row, phase angle distributions of the waves (Methods). Lower row, distributions of local order parameter calculated based on the phase distributions (Methods). Colour bars to the right of the middle and lower rows indicate the magnitude of phase angle and local order parameter, respectively. Scale bar, 500 μm. Also see Supplementary Video 2. $T = 0$ min marks the onset of segmented and disordered wavefronts. **d**, Space–time trajectories of spiral cores during the development of spiral waves associated with the representative case shown in **c**. The nearly straight trajectories in this three-dimensional plot at time >~20 min indicate that the spiral cores are almost stationary. **e**, Standard deviation (s.d.) of the local oscillation period distribution plotted against time in a representative experiment shown in **c**. Inset, histograms showing the probability distribution of the local oscillation period at time = 10 min and 70 min.

pilus motor activity is essential for the wave generation, as *P. aeruginosa* strains with defect in type-IV pilus motility (either not producing type IV pili (PA14 *flgk::Tn5 ΔpilA*) or not being able to retract and generate mechanical forces (PA14 *flgk::Tn5 ΔpilY1*) (Methods)) failed to form the propagating spiral waves.

To follow the onset and evolution of the propagating spiral waves, we prepared disk-shaped artificial bacterial films ~20–30 μm in thickness and densely packed with a homogeneous population of *P. aeruginosa* cells (Methods). The solid-like artificial bacterial film also displays propagating spiral waves, and more importantly, it allows us to exclude the effect of behavioural heterogeneity in naturally developed bacterial colonies. Using this experimental system, we found a self-organization process during the formation of the spiral wave. In the beginning, some sporadic domains with segmented and disordered wavefronts appeared in the artificial bacterial films (Fig. 1c, upper row and Supplementary Video 2). These disordered wavefronts spontaneously emerged; subsequently they coalesced, interconnected and eventually turned into propagating spiral waves. To understand the spatiotemporal ordering process of the local light-intensity oscillations, we defined the instantaneous period of the wave at a specific location as the time interval between two consecutive wavefronts passing this location, and used this information to compute the phase of local oscillations (setting the phase at the wavefronts seen in phase-contrast images as zero) (Methods). The phase distribution allows us to calculate the local order parameter $\chi(\mathbf{r})$ commonly adopted to describe synchronization behaviour and defined as $\chi(\mathbf{r})\, e^{i\bar{\theta}} = \frac{1}{N}\sum_s e^{i\theta}$ [2,23], where $\bar{\theta}$ is the local average of phase angle (θ) of oscillators within a local circular area s centred at $\mathbf{r}$ and N is the total number of oscillators within the local circular area (Methods). As shown by distributions of the phase and the local order parameter (Fig. 1c, middle and lower rows and Supplementary Video 2), the phases of local light-intensity oscillations self-organized in space from a disordered state to a highly ordered state with the spiral wave pattern.

Moreover, after the wave form stabilized, the spiral cores (or spiral centres) specified by the local minima of local order parameter[6] did not display any meandering motion seen in many other systems with propagating spiral waves[24]; instead, they appeared to be stationary (Supplementary Video 2), with a negligible core diffusivity as low as 6.92 $\mu m^2\, min^{-1}$ or equivalently 4.80×10^{-5} square wavelengths per period (wavelength ~0.99 mm) (Fig. 1d, Extended Data Figs. 1 and 2 and

https://doi.org/10.1038/s41567-024-02457-5

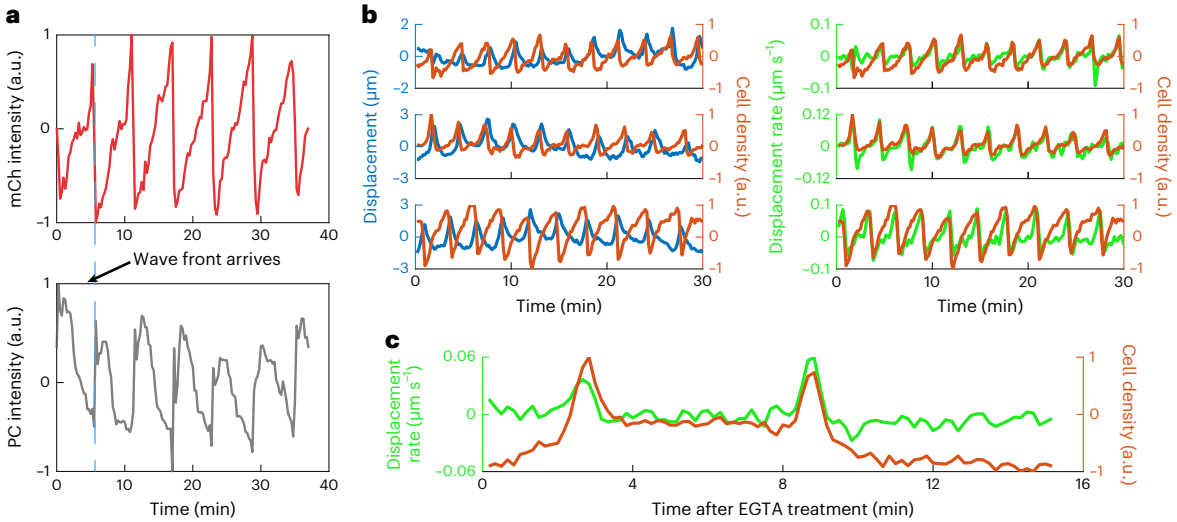

Fig. 2 | Analysis of cell density variation and single-cell displacement reveals propagating tension waves. a, Periodic variation of local cell density during spiral wave propagation (representative experiment). For a small region (~32.5 μm × 32.5 μm) arbitrarily selected from artificial bacterial films of mCherry-labelled *P. aeruginosa* that display propagating spiral waves, the fluorescence intensity of mCherry (mCh, upper panel) exhibits periodic oscillation coinciding with the light-intensity oscillation in phase-contrast (PC) channel (lower panel). Dashed line indicates one of the instants when the wavefront arrives at the chosen position. The fluorescence intensity adjacent to the left of the dashed line corresponds to cell density just before the wavefront arrives, and thus it represents the cell density in front of the wavefront (denoted as leading side in main text) in a reference frame co-moving with the wavefront; conversely, the fluorescence intensity adjacent to the right of the dashed line represents the cell density behind the wavefront (denoted as lagging side). **b**, Oscillatory forth-and-back displacement of individual cells and local cell density variation during spiral wave propagation. Traces measured with three representative cells from different experiments are presented. For each cell, the time trace of displacement (blue lines; left panel) or the rate of displacement (green lines; right panel) are overlaid by the time trace of local cell density (red lines) measured as the fluorescent intensity in the area associated with the cell (Methods). The time-averaged cross-correlation between displacement and cell density for the three traces in the left panel is: −0.03, 0.08 and 0.17, respectively (upper to lower); the cross-correlation between displacement rate and cell density for the three traces is 0.71, 0.86 and 0.71, respectively. **c**, Forth-and-back displacement of individual cells and local cell density variation during the propagation of train waves triggered by EGTA treatment in a representative experiment. The rate of displacement (green line) is overlaid by the time trace of local cell density (red line) measured as the fluorescent intensity in the area associated with the cell (Methods). The EGTA filter disk was applied to the bacterial film at time = 0 min.

Methods). We further calculated instantaneous oscillation period at all positions during the spiral wave development and found that the spatial distribution of period gradually homogenized during the emergence of the spiral waves (Fig. 1e and Extended Data Fig. 3, lower row). To summarize, the ordering of phase distribution and the homogenization of local oscillation period together demonstrate a synchronization process that leads to formation of the propagating spiral waves with remarkable temporal stability.

Spiral waves manifest spatiotemporal order of tension force

The observed light-intensity oscillation in the phase-contrast images presumably reflects the variation of surface-packing cell density in the quasi-two-dimensional bacterial living matter. To examine this notion, we labelled *P. aeruginosa* cells with the fluorescent protein mCherry and measured cell density via fluorescence imaging (Methods). We found that the mCherry fluorescence intensity (a proxy of local cell density) exhibits the same propagating spiral wave pattern that coincides with the wave observed in phase-contrast images (Supplementary Video 3). Cell density at the leading side of the wavefront is higher than that at the lagging side (Fig. 2a and Supplementary Video 3); also during one wave period, the cell density at a specific location first increases as a wavefront approaches and then drops abruptly as the wavefront moves away (Fig. 2a). The observed propagating spiral waves thus reflect periodic variation of cell density.

To understand the origin of the cell density variation in the bacterial film, we tracked the movement of cells by labelling a small fraction of the population (0.1%) with mCherry fluorescent protein (Methods). We found that cells appeared to displace gradually toward the wave propagating direction together with the approaching wavefronts for a distance of several μm, and then they rapidly returned to their original position after the wavefronts had passed (Fig. 2b, left and Supplementary Video 4). These results suggest that the cell density variation is associated with periodic forth-and-back displacement of cells that causes in-plane deformation of the bacterial film. Therefore, the wave resembles a longitudinal or acoustic wave seen in passive elastic materials; here cells serve as an active medium that not only mediates wave propagation but also self-generates the wave through pilus motor activity. Interestingly, while the displacement of cells lagged behind the density variation (Fig. 2b, left), the time rate of cell displacement was well synchronized with the density variation (Fig. 2b, right). Our theoretical analysis of displacement field shows that this result is a direct consequence of mass conservation in the bacterial film (Methods).

The local forth-and-back displacement of cells associated with the cell density variation displayed negligible net displacement during a cycle, suggesting local force imbalance in the bacterial film. To analyse the forces in the bacterial film, we modelled the bacterial film as an elastic medium in which the elastic force and substrate friction competes with an internal tension that arises from the pulling forces generated by pilus retraction (Methods). We found that the variation of tension force inside the bacterial film is in phase with the variation in local cell density (Methods). In other words, the observed spiral waves of density variation shown in Fig. 2a are in fact propagating tension waves in the bacterial film, with cells at the leading side of the wavefront experiencing a higher pilus-generated tension than the lagging side. This pattern of propagating tension waves would require spatiotemporal coordination of pilus motor activity in mass elements of the bacterial film. For example, the average pilus retraction probability should be higher at the leading side and lower at the lagging side of the wavefront. In particular, the rapid restoring displacement

of cells when wavefronts pass by indicates that pilus motors have by then completed retraction synchronously.

Synchronized pilus activity drives the tension wave

To examine whether coordination of bacterial pilus motor activity underlies the propagating tension waves, we sought to manipulate the waves by treating the bacterial films with drugs that alter pilus motor activity. Ethylene glycol tetraacetic acid (EGTA) is a calcium chelator that was previously reported to cause pilus retraction[25,26]. When a filter paper disc soaked with EGTA (Methods) was placed onto a bacterial film before the emergence of segmented and disordered wavefronts (Fig. 1c), we found that a train of waves emanated from near the edge of the filter paper disc and propagated outwards, which displayed similar local dynamics of cell density variation and forth-and-back motion pattern as seen in the naturally emerged propagating tension waves (Fig. 2c and Supplementary Video 5). In bacterial films with pre-existing propagating tension waves, the EGTA treatment abolished the original wave pattern near the filter disk, followed by the emergence of a similar wave train initiated near the edge of the filter disk (Supplementary Video 5). In addition, we found that filter discs containing other drugs that were reported to cause pilus retraction (trifluoperazine and thioridazine[26]) also triggered train waves (Supplementary Video 6). Interestingly, a diffusion pulse of extracellular ATP (eATP) showed a similar effect in exciting train waves (Supplementary Video 6); eATP was reported to inhibit pilus motility and may also reset the phase of the cyclic force-generating process, although it is unclear whether it causes pilus retraction or inhibits pilus extension[27].

These results can be understood as follows. Cells near the filter disk experience a rapid diffusion pulse of the drug (for example, EGTA), and the type IV pili of cells that encounter the drug concentration pulse will simultaneously retract. The simultaneous pilus retraction would reset the phase of the cyclic force-generating process of pili and force the synchronization of these cycles, thus triggering the train waves. Therefore, these results provide strong evidence that the propagating tension waves results from spatiotemporal coordination of pilus motor activity. The coordination or coupling of pilus activities is presumably mediated by the mechanosensing pathways of cells, as type-IV pilus motility is actively coupled to the mechanical environment[28–33].

A non-reciprocal oscillator model reproduces the spiral waves

Next we seek to understand how spatiotemporal coordination of pilus retraction–extension cycle could give rise to the propagating spiral tension waves. Although methods to visualize type IV pili have been developed for isolated cells[20–22,34], direct observation of pilus activity in densely packed cell layers is technically challenging. Here we resort to mathematical modelling and adopt the framework of Kuramoto model[2] well-known for the study of synchronization phenomena. We considered mass elements in the bacterial film as a system of spatially coupled oscillators on a two-dimensional square lattice (Fig. 3a). Each oscillator describes the pilus retraction–extension cycle represented by a phase angle θ ($\theta \in [0, 2\pi]$), which is proportional to the probability that the pilus motors of cells in a mass element entering the retraction or force-generating state; for example, $\theta = 0$ corresponds to the state that none of the pilus motors is retracting and thus the mass element does not exert pilus-mediated forces to the environment. As the pilus retraction–extension cycle can only proceed forward but not backward[35], a key ingredient of our model is that an oscillator is more likely to accelerate than to decelerate its phase during interaction with its neighbours, that is the bacterial pilus activities are coupled in a non-reciprocal manner. Specifically, we introduce isotropic non-reciprocal coupling to the locally coupled two-dimensional Kuramoto model as follows (Fig. 3a and Methods):

$$\frac{\mathrm{d}\theta_{(i,j)}}{\mathrm{dt}} = \omega_{0(i,j)} + \frac{\kappa}{N}\sum_{r\le l}\left[\sin(\theta_{(m,n)} - \theta_{(i,j)})F\left(\sin\left(\theta_{(m,n)} - \theta_{(i,j)}\right)\right)\right] + \eta(t). \quad (1)$$

Here $\theta_{(i,j)}$ is the phase angle of the oscillator at the location (i,j); $\omega_{0(i,j)}$ is the intrinsic angular frequency of the oscillator located at (i,j); $r = \sqrt{(m-i)^2 + (n-j)^2}$ is the spatial distance between two oscillators at point (m,n) and (i,j); l denotes the coupling range; κ is the coupling strength; and $\eta(t)$ is a Gaussian white noise (Methods). The step function $F(x)$ in the coupling term is defined as: $F(x) = (1-\varepsilon)/2$, for $x < 0$; $F(x) = (1+\varepsilon)/2$, for $x \ge 0$, with $\varepsilon \in [0, 1]$ being a measure of non-reciprocity. This is the simplest form of isotropic, non-reciprocal coupling (Methods).

In addition to the Kuramoto dynamics for the phase oscillators described above, we allow the mass elements to be displaced due to external forces (including pilus-driven tension force, elastic force and friction force; Methods). The displacement of mass elements changes the relative distance between neighbouring phase oscillators and thereby may modify the coupling dynamics between these locally coupled oscillators. Taking the tension T generated by a mass element to be proportional to the phase angle θ associated with the mass element, the two-dimensional displacement field $\mathbf{d}(x,y,t) = (d_1, d_2)$ of the bacterial film can be solved numerically and the cell density distribution $\rho(x,y,t)$ can be obtained by $\rho \propto -\nabla \cdot \mathbf{d}$ (Methods).

We performed numerical simulations of the non-reciprocal coupled-oscillator model based on equation (1) on a finite homogeneous domain (Methods) with $\varepsilon > 0$. Starting from initially random distributions of phase angle and intrinsic angular frequency (Methods), we found that the system self-organizes into a highly ordered state that displays periodically propagating spiral waves at any level of non-reciprocity. For the case with full non-reciprocity ($\varepsilon = 1$, which better describes the coupling of bacterial pilus activities), the evolutionary process of the spiral wave pattern faithfully reproduces the dynamics observed in experiments (Fig. 3b–e and Supplementary Video 7), including the spatial homogenization of instantaneous angular frequency (Extended Data Fig. 4) and the stability of spiral cores (with a negligible spiral core diffusivity of 6.14×10^{-4} square wavelengths per period; Fig. 3f and Extended Data Fig. 2). By contrast, without non-reciprocal coupling (that is, setting $\varepsilon = 0$), equation (1) becomes the familiar Kuramoto model that does not spontaneously generate stable spiral waves in a homogeneous system. We note that another modified Kuramoto model could produce propagating spiral waves by introducing a time delay in the coupling function[36]; however, the spiral wave there was less stable, with the spiral cores displaying apparent motion. We further found that forced synchronization of oscillators in certain area triggers travelling train waves that emanate from the area's boundary and eliminates pre-existing spiral waves outside the area (Extended Data Fig. 5, Supplementary Video 8 and Methods). The results reproduce the phenomena when artificial bacterial films were treated by drugs causing pilus retraction (Supplementary Videos 5 and 6), and are similar to the unpinning process of spiral waves previously reported in Belousov–Zhabotinsky reactions and cardiac tissues[37]. Taken together, the remarkable agreement between our simulations and experiments supports that non-reciprocal coupling of pilus activities is key to the emergence of the observed propagating spiral waves.

Stability of the spiral wave depends on non-reciprocity

An important feature of the propagating spiral waves found in our experiments is that the spiral cores are stationary, which is reproduced by our simulations described above. To further understand the stability of spiral cores, we followed the evolutionary dynamics of spiral waves in simulations. We found that the number density of spiral cores

https://doi.org/10.1038/s41567-024-02457-5

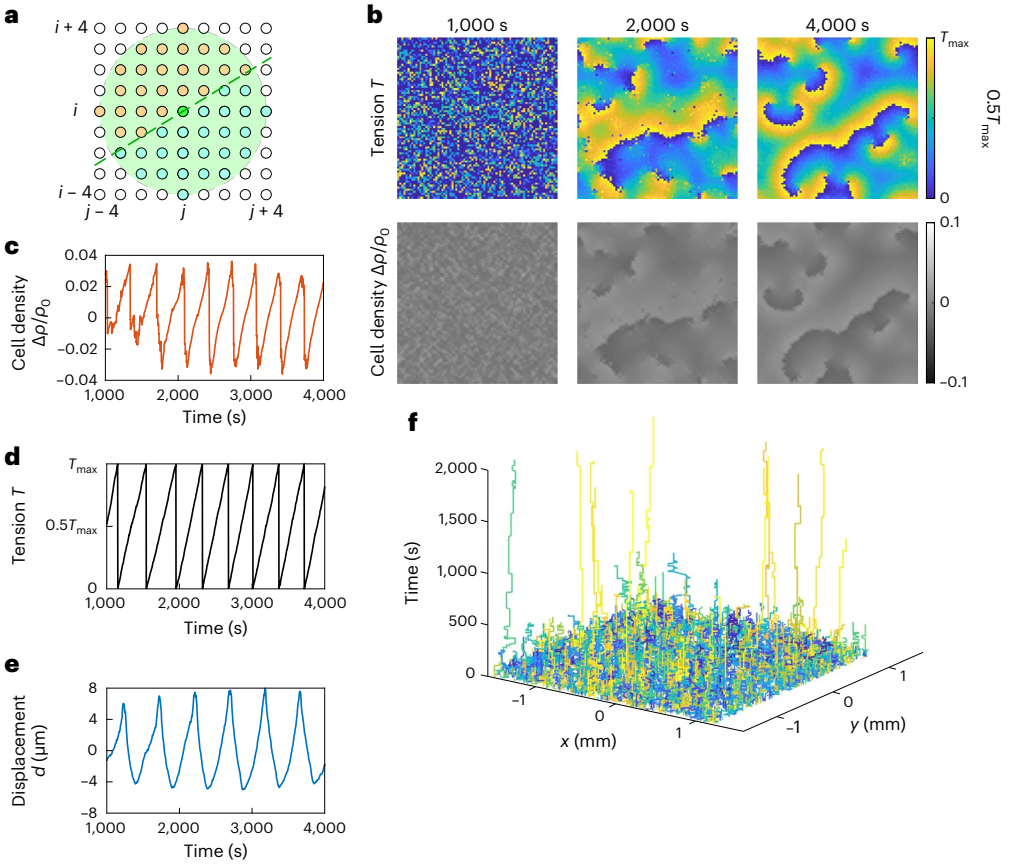

Fig. 3 | Coupled-oscillator model with non-reciprocal interaction reproduces the observed propagating spiral waves. a, Schematic diagram of the locally coupled two-dimensional Kuramoto model with isotropic non-reciprocal coupling. The nearest neighbour distance between the oscillators (represented as circles) is d. For the oscillator located at position (i,j) at the centre of the diagram, the green-shaded circular area with radius $l = 4d$ represents the coupling range. Assuming that the wavefront (that is, equi-phase line indicated by the green dashed line) propagates towards the upper left corner, the oscillators labelled in blue colour phase-lead oscillator (i,j) and accelerate it, while those labelled in orange colour lag behind oscillator (i,j) and decelerate it. According to the summation in equation (1), the total magnitude of acceleration is greater than that of deceleration. **b**, Spatiotemporal dynamics of tension field (T) and cell density ($\Delta\rho/\rho_0$) distribution in simulations with a full non-reciprocity $\varepsilon = 1$ showing the development of propagating spiral waves. The system consists of 80 × 80 oscillators. **c**–**e**, Simulated temporal dynamics of cell density (**c**), tension (**d**) and displacement (d) (**e**) at an arbitrarily selected mass element during spiral wave propagation $T_{max} = 81$ Pa in **d** (Methods). **f**, Space–time trajectories of spiral cores during the development of spiral waves associated with **b** plotted in the same manner as Fig. 1d.

increases with the level of non-reciprocity; at lower non-reciprocity, nearby pairs of spiral cores with opposite topological charges (+1 or −1 for counterclockwise or clockwise rotating spiral waves) tend to annihilate at a higher rate during the developmental process, thus leaving less cores when the spiral wave pattern stabilizes (Fig. 4a and Supplementary Video 9). To understand this behaviour, we would like to study pairwise interaction between spiral cores systematically in the model. We note that the dynamics of spiral cores in the model is barely affected by oscillator displacement; this observation can be understood as arising from the fact that the displacement of mass elements (a few microns; Fig. 3e) is 1–2 orders of magnitude smaller than the coupling range set in the model (160 μm, which is required to reproduce the wavelength of spiral wave patterns found in experiments; Methods). Therefore, for the sake of generality, we now fix the position of oscillators in the model and study spiral core dynamics with the non-reciprocal Kuramoto model (equation (1)) alone.

We artificially create two counter-rotating Archimedean spiral wave patterns (that is the equi-phase lines of the oscillators being described by $\rho \propto \phi$, where ρ and ϕ are the radius and polar angle in polar coordinates, respectively)[3] with their cores separated by a variable distance; note that, a pair of spiral waves with identical rotating chirality will not annihilate due to the general requirement of topological charge conservation[38]. Remarkably, we find that the pair of opposite-charge spiral cores experience short-range attraction and intermediate-range repulsion for all non-reciprocity $\varepsilon > 0$; as the level of non-reciprocity increases, the attraction range shrinks while the repulsion range expands (Fig. 4b). As a consequence, opposite-charge spiral cores would tend to avoid getting too close to each other at larger non-reciprocity, thus maintaining stability during the development of spiral wave patterns.

We stress that the emergence of propagating spiral waves observed in pilus-driven bacterial living matter does not rely on spatial inhomogeneity, in contrast to spiral waves in chemical excitable media[39]. Nonetheless, we sought to understand how spatial inhomogeneity or defects would perturb the wave dynamics. To examine this question, we created a hollow area with inactivated oscillators (representing a spatial defect inert to oscillator interactions) in the simulation (Methods). We found that the wave morphology was only affected very close to the defect (Fig. 4c and Supplementary Video 10), which is confirmed by laser ablation experiment (Supplementary Video 11 and Methods). Therefore, the global spiral wave pattern is resilient to spatial inhomogeneity.

Discussion

In summary, we have discovered a novel spiral wave pattern in the bacterial world: Synchronization of type-IV pilus motility in bacterial

https://doi.org/10.1038/s41567-024-02457-5

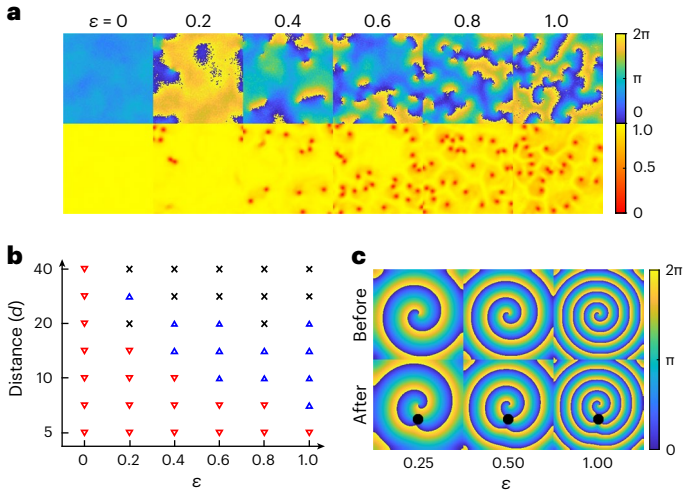

Fig. 4 | Effect of non-reciprocity and spatial inhomogeneity on the stability of spiral wave pattern. a, Spiral wave patterns formed with different levels of non-reciprocity in simulations of the coupled-oscillator model. The spatial distributions of phase angle (upper) and local order parameter (lower) at time = 4,000 s are shown for the corresponding level of non-reciprocity ε indicated on top of the figures. **b**, Phase map of pairwise-interaction mode between spiral cores on the plane of non-reciprocity (ε) and core-core distance (in unit of nearest oscillator distance d). For a given ε, the pair of spiral cores may move towards each other (∇), repel from each other (Δ) or display no relative motion (×), depending on their distance. **c**, Resilience of spiral waves to spatial inhomogeneity. This panel shows the steady-state spatial distributions of phase angle before (upper row) and after (lower row) introducing a hollow-like spatial defect in the simulation domain (black solid circle), where the oscillators are inactivated and do not interact with others (Methods).

living matter gives rise to a large-scale propagating spiral waves of tension force. Using numerical simulations of a locally coupled-oscillator model, we show that non-reciprocal coupling between the pilus motor activities underlies the emergence of the spiral wave pattern.

For many systems out of equilibrium, including living matter and synthetic active matter, the interaction between their elementary units is often non-reciprocal[40–43], that is violating the action–reaction principle of Newton's third law. Recently non-reciprocity has been suggested to drive phase transition and self-organization in active matter[43,44]. In this connection, it is intriguing that non-reciprocity controls wave dynamics during the synchronization of coupled oscillators. Our results may shed light on the collective dynamics in other living and active matter systems with cyclic force-generating processes[45–47].

Most mechanisms for the onset of spiral waves require external stimulation[39], spatial inhomogeneity[39] or special initial conditions[6,48]. By contrast, our results suggest that non-reciprocity provides a simple mechanism for the spontaneous formation of stable spiral waves in homogeneous media without external stimuli. An important feature of the bacterial spiral wave pattern reported here is that the spiral cores are nearly stationary at steady state. This characteristic is shared by certain types of electrical and chemical spiral waves found in oocyte cytoplasm[17], eukaryotic cell cortex[18] and cardiac tissues[7,10]. The bacterial spiral wave pattern may therefore serve as a tractable mechanical analogue for investigating the origin and control of stable spiral waves in diverse living systems.

Online content

Any methods, additional references, Nature Portfolio reporting summaries, source data, extended data, supplementary information, acknowledgements, peer review information; details of author contributions and competing interests; and statements of data and code availability are available at https://doi.org/10.1038/s41567-024-02457-5.

References

1. Cross, M. C. & Hohenberg, P. C. Pattern formation outside of equilibrium. *Rev. Mod. Phys.* **65**, 851–1112 (1993).
2. Kuramoto, Y. *Chemical Oscillations, Waves, and Turbulence* (Dover Publications, 2003).
3. Winfree, A. T. *The Geometry of Biological Time* (Springer-Verlag, 2001).
4. Zaikin, A. N. & Zhabotinsky, A. M. Concentration wave propagation in two-dimensional liquid-phase self-oscillating system. *Nature* **225**, 535–537 (1970).
5. Jakubith, S., Rotermund, H. H., Engel, W., von Oertzen, A. & Ertl, G. Spatiotemporal concentration patterns in a surface reaction: propagating and standing waves, rotating spirals, and turbulence. *Phys. Rev. Lett.* **65**, 3013–3016 (1990).
6. Totz, J. F., Rode, J., Tinsley, M. R., Showalter, K. & Engel, H. Spiral wave chimera states in large populations of coupled chemical oscillators. *Nat. Phys.* **14**, 282–285 (2018).
7. Davidenko, J. M., Pertsov, A. V., Salomonsz, R., Baxter, W. & Jalife, J. Stationary and drifting spiral waves of excitation in isolated cardiac muscle. *Nature* **355**, 349–351 (1992).
8. Huang, X. et al. Spiral wave dynamics in neocortex. *Neuron* **68**, 978–990 (2010).
9. Jalife, J. Ventricular fibrillation: mechanisms of initiation and maintenance. *Annu. Rev. Physiol.* **62**, 25–50 (2000).
10. Narayan, S. M., Patel, J., Mulpuru, S. & Krummen, D. E. Focal impulse and rotor modulation ablation of sustaining rotors abruptly terminates persistent atrial fibrillation to sinus rhythm with elimination on follow-up: a video case study. *Heart Rhythm* **9**, 1436–1439 (2012).
11. Tomchik, K. J. & Devreotes, P. N. Adenosine 3′,5′-monophosphate waves in Dictyostelium discoideum: a demonstration by isotope dilution-fluorography. *Science* **212**, 443–446 (1981).
12. Takagi, S. & Ueda, T. Emergence and transitions of dynamic patterns of thickness oscillation of the plasmodium of the true slime mold Physarum polycephalum. *Physica D* **237**, 420–427 (2008).
13. Mattick, J. S. Type IV Pili and twitching motility. *Annu. Rev. Microbiol.* **56**, 289–314 (2002).
14. Burrows, L. L. Pseudomonas aeruginosa twitching motility: type IV pili in action. *Annu. Rev. Microbiol.* **66**, 493–520 (2012).
15. Maier, B., Potter, L., So, M., Seifert Hank, S. & Sheetz Michael, P. Single pilus motor forces exceed 100 pN. *Proc. Natl Acad. Sci. USA* **99**, 16012–16017 (2002).
16. Nijjer, J. et al. Mechanical forces drive a reorientation cascade leading to biofilm self-patterning. *Nat. Commun.* **12**, 6632 (2021).
17. Lechleiter, J., Girard, S., Peralta, E. & Clapham, D. Spiral calcium wave propagation and annihilation in Xenopus laevis oocytes. *Science* **252**, 123–126 (1991).
18. Bement, W. M. et al. Activator–inhibitor coupling between Rho signalling and actin assembly makes the cell cortex an excitable medium. *Nat. Cell Biol.* **17**, 1471–1483 (2015).
19. Merz, A. J., So, M. & Sheetz, M. P. Pilus retraction powers bacterial twitching motility. *Nature* **407**, 98–102 (2000).
20. Skerker, J. M. & Berg, H. C. Direct observation of extension and retraction of type IV pili. *Proc. Natl Acad. Sci. USA* **98**, 6901–6904 (2001).
21. Talà, L., Fineberg, A., Kukura, P. & Persat, A. Pseudomonas aeruginosa orchestrates twitching motility by sequential control of type IV pili movements. *Nat. Microbiol.* **4**, 774–780 (2019).
22. Koch, M. D., Fei, C., Wingreen, N. S., Shaevitz, J. W. & Gitai, Z. Competitive binding of independent extension and retraction motors explains the quantitative dynamics of type IV pili. *Proc. Natl Acad. Sci. USA* **118**, e2014926118 (2021).
23. Strogatz, S. H. From Kuramoto to Crawford: exploring the onset of synchronization in populations of coupled oscillators. *Physica D* **143**, 1–20 (2000).

24. Barkley, D. in *Chemical Waves and Patterns* (eds R. Kapral & K. Showalter) 163–189 (Springer, 1995).
25. Orans, J. et al. Crystal structure analysis reveals Pseudomonas PilY1 as an essential calcium-dependent regulator of bacterial surface motility. *Proc. Natl Acad. Sci. USA* **107**, 1065–1070 (2010).
26. Denis, K. et al. Targeting type IV pili as an antivirulence strategy against invasive meningococcal disease. *Nat. Microbiol.* **4**, 972–984 (2019).
27. Nolan, L. M., Cavaliere, R., Turnbull, L. & Whitchurch, C. B. Extracellular ATP inhibits twitching motility-mediated biofilm expansion by Pseudomonas aeruginosa. *BMC Microbiol.* **15**, 55 (2015).
28. Maier, B. & Wong, G. C. L. How bacteria use type IV pili machinery on surfaces. *Trends Microbiol.* **23**, 775–788 (2015).
29. Persat, A., Inclan Yuki, F., Engel, J. N., Stone, H. A. & Gitai, Z. *Proc. Natl Acad. Sci. USA* **112**, 7563–7568 (2015).
30. Sabass, B., Koch, M. D., Liu, G., Stone, H. A. & Shaevitz, J. W. Force generation by groups of migrating bacteria. *Proc. Natl Acad. Sci. USA* **114**, 7266–7271 (2017).
31. Rodesney, C. A. et al. Mechanosensing of shear by Pseudomonas aeruginosa leads to increased levels of the cyclic-di-GMP signal initiating biofilm development. *Proc. Natl Acad. Sci. USA* **114**, 5906–5911 (2017).
32. Kühn, M. J. et al. Mechanotaxis directs Pseudomonas aeruginosa twitching motility. *Proc. Natl Acad. Sci. USA* **118**, e2101759118 (2021).
33. Koch Matthias, D., Black Matthew, E., Han, E., Shaevitz Joshua, W. & Gitai, Z. Pseudomonas aeruginosa distinguishes surfaces by stiffness using retraction of type IV pili. *Proc. Natl Acad. Sci. USA* **119**, e2119434119 (2022).
34. Ellison Courtney, K. et al. Obstruction of pilus retraction stimulates bacterial surface sensing. *Science* **358**, 535–538 (2017).
35. Maier, B., Koomey, M. & Sheetz, M. P. A force-dependent switch reverses type IV pilus retraction. *Proc. Natl Acad. Sci. USA* **101**, 10961–10966 (2004).
36. Kim, P.-J., Ko, T.-W., Jeong, H. & Moon, H.-T. Pattern formation in a two-dimensional array of oscillators with phase-shifted coupling. *Phys. Rev. E* **70**, 065201 (2004).
37. Tanaka, M. et al. Unpinning of a spiral wave anchored around a circular obstacle by an external wave train: Common aspects of a chemical reaction and cardiomyocyte tissue. *Chaos* **19**, 043114 (2009).
38. Davidsen, J., Glass, L. & Kapral, R. Topological constraints on spiral wave dynamics in spherical geometries with inhomogeneous excitability. *Phys. Rev. E* **70**, 056203 (2004).
39. Zykov, V. S. Spiral wave initiation in excitable media. *Philos. Trans. R. Soc. A* **376**, 20170379 (2018).
40. Nagy, M., Ákos, Z., Biro, D. & Vicsek, T. Hierarchical group dynamics in pigeon flocks. *Nature* **464**, 890–893 (2010).
41. Ivlev, A. V. et al. Statistical Mechanics where Newton's Third Law is Broken. *Phys. Rev. X* **5**, 011035 (2015).
42. Lavergne, F. A., Wendehenne, H., Bäuerle, T. & Bechinger, C. Group formation and cohesion of active particles with visual perception-dependent motility. *Science* **364**, 70–74 (2019).
43. Fruchart, M., Hanai, R., Littlewood, P. B. & Vitelli, V. Non-reciprocal phase transitions. *Nature* **592**, 363–369 (2021).
44. You, Z., Baskaran, A. & Marchetti, M. C. Nonreciprocity as a generic route to traveling states. *Proc. Natl Acad. Sci. USA* **117**, 19767–19772 (2020).
45. Uchida, N. & Golestanian, R. Synchronization and collective dynamics in a carpet of microfluidic rotors. *Phys. Rev. Lett.* **104**, 178103 (2010).
46. Bull, M. S., Prakash, V. N. & Prakash, M. Ciliary flocking and emergent instabilities enable collective agility in a non-neuromuscular animal. Preprint at *arXiv* https://arxiv.org/abs/2107.02934 (2021).
47. Chakrabarti, B., Shelley, M. J. & Fürthauer, S. Collective motion and pattern formation in phase-synchronizing active fluids. *Phys. Rev. Lett.* **130**, 128202 (2023).
48. Zhang, H., Hu, B., Hu, G., Ouyang, Q. & Kurths, J. Turbulence control by developing a spiral wave with a periodic signal injection in the complex Ginzburg-Landau equation. *Phys. Rev. E* **66**, 046303 (2002).

Methods

Experimental procedures and data analysis

The following strains were used: piliated *P. aeruginosa* PA14 ZK3367 (PA14 *flgK*::Tn5; without flagellar motility but retaining type-IV pilus motility; primarily used in this study), gift from Roberto Kolter, Harvard University[49]; *P. aeruginosa* PA14 ZK3367 labelled by GFP (PA14 *flgK*::Tn5 transformed with a plasmid pMHLB P_{lasB}-gfp(ASV) Gen^R (ref. 50) by electroporation; the plasmid was a gift from Liang Yang at Southern University of Science and Technology); *P. aeruginosa* PA14 ZK3367 with constitutive expression of mCherry in cytoplasm (PA14 *flgK*::Tn5 transformed with a pJN105-mCherry Gen^R plasmid (gift from Fan Jin at Shenzhen Institute of Advanced Technology) by electroporation); non-motile *P. aeruginosa* without either flagellar or type-IV pilus motility (PA14 *flgk::Tn5 ΔpilA*, which does not produce type IV pili; and PA14 *flgk::Tn5 ΔpilY1*, which is not able to retract and generate mechanical forces)[51], gifts from George A. O'Toole, Dartmouth College; *P. aeruginosa* PA14 ZK3367 deficient in PelA matrix production (PA14 *flgK*::Tn5 Δ*pelA*) or deficient in rhamnolipid production (PA14 *flgK*::Tn5 Δ*rhlA*)[52]. Single-colony isolates were grown overnight (all for ~13–14 hr, except the strain harbouring pJN105-mCherry plasmid that requires ~16 hr growth) in 10 ml culture tubes (unless otherwise stated) with shaking in LB medium (1% Bacto tryptone, 0.5% yeast extract, 0.5% NaCl) at 30 °C to stationary phase. For cultures of strains harbouring plasmids expressing GFP or mCherry, the antibiotic gentamycin was added to a final concentration 50 μg ml^{-1} in the LB broth. Overnight cultures were used for inoculating colonies on agar plates.

Colonies or disk-shaped artificial bacterial films of *P. aeruginosa* were grown on 0.5% Difco Bacto agar plates infused with M9DCAA medium[53] (20 mM NH_4Cl, 12 mM Na_2HPO_4, 22 mM KH_2PO_4, 8.6 mM NaCl, 1 mM $MgSO_4$, 1 mM $CaCl_2$, 11 mM dextrose and 0.5% (weight per volume) casamino acids (BD Bacto, catalogue no. 223050)). As Ca^{2+} cannot coexist stably with many ions, this medium was prepared and stored in two components: (1) ×10 nutrient solution without $CaCl_2$, sterilized and stored at room temperature; (2) agar infused with $CaCl_2$ at $1\frac{1}{9}\times$ of the desired concentrations, sterilized and stored in 100 ml aliquots. Before use, the component (2) was melted completely in a microwave oven and cooled to ~50–60 °C. For each plate, 18 ml molten component (2) was mixed with 2 ml component (1), and the mixture was poured to a polystyrene petri dish (90 mm diameter, 15 mm height). The M9DCAA agar plate was swirled gently to ensure surface flatness, followed by further drying under laminar airflow for 20 min at room temperature.

The detailed procedures of sample preparation, sample manipulation, image acquisition, image processing and data analysis and rheological measurement are included in the Supplementary Methods. In addition to the propagating spiral waves observed in piliated *P. aeruginosa* PA14 (PA14 *flgK*::Tn5) that was primarily used in this study, similar spiral wave pattern was observed with a piliated *P. aeruginosa* PA14 mutant lacking the major extracellular matrix component Pel[54] (PA14 *flgK*::Tn5 Δ*pelA*). The spiral waves were also observed with a rhamnolipid-deficient piliated *P. aeruginosa* PA14 mutant (PA14 *flgK*::Tn5 Δ*rhlA*), thus excluding the contribution of interfacial flows to the phenomenon.

Theoretical analysis of displacement and tension fields in the bacterial film

General relation between spatial and temporal derivatives in propagating waves. Without loss of generality, we define the positive x-axis direction as the local wave propagating direction. Any mechanical variable Γ (for example, the displacement, speed, tension, surface-packing cell density, oscillation phase angle and so on) that periodically changes in time can be described as a function of phase angle θ (in the range of $[0, 2\pi]$). As $\theta(x,t)$ can be expressed in terms of $(x-v_0t)$ as $\theta_{(x-v_0t)}$, where v_0 is the wave speed and it is assumed to be a constant for a stable periodically propagating wave, we have:

$$\Gamma(x,t) = \Gamma(\theta) = \Gamma\left(\theta_{(x-v_0t)}\right). \tag{2}$$

Then we have:

$$\begin{aligned}\frac{\partial\Gamma}{\partial x} &= \frac{\mathrm{d}\Gamma}{\mathrm{d}}\frac{\partial\theta}{\partial x} = \frac{\mathrm{d}\Gamma}{\mathrm{d}}\frac{\mathrm{d}\theta}{\mathrm{d}(x-v_0t)}\frac{\partial(x-v_0t)}{\partial x} = \frac{\mathrm{d}\Gamma}{\mathrm{d}}\frac{\mathrm{d}\theta}{\mathrm{d}(x-v_0t)},\\ \frac{\partial\Gamma}{\partial t} &= \frac{\mathrm{d}\Gamma}{d\theta}\frac{\partial\theta}{\partial t} = \frac{\mathrm{d}\Gamma}{\mathrm{d}\theta}\frac{\mathrm{d}\theta}{\mathrm{d}(x-v_0t)}\frac{\partial(x-v_0t)}{\partial t} = -v_0\frac{\mathrm{d}\Gamma}{\mathrm{d}\theta}\frac{\mathrm{d}\theta}{\mathrm{d}(x-v_0t)}\end{aligned}. \tag{3}$$

Comparing the form of $\frac{\partial\Gamma}{\partial x}$ and $\frac{\partial\Gamma}{\partial t}$, we have:

$$\frac{\partial\Gamma}{\partial x} = -\frac{1}{v_0}\frac{\partial\Gamma}{\partial t}. \tag{4}$$

Thus, we can replace the operator $\frac{\partial}{\partial x}$ by $-\frac{1}{v_0}\frac{\partial}{\partial t}$ in the following calculation. Meanwhile, as we have chosen the positive x-axis direction as the propagating direction of the wave, the y-axis direction is parallel to the wavefront where the oscillation phases θ are in sync. Thus, Γ should not vary in y-axis direction and we have: $\frac{\partial\Gamma}{\partial y} = 0$.

Displacement field analysis. The total biomass in a mass element of the quasi-two-dimensional bacterial film with surface area S_0 and surface cell density ρ_0 is proportional to $\rho_0 S_0$. Due to biomass conservation, we have the following relation between small variations in the surface area ($\Delta S \equiv S - S_0$) and cell density ($\Delta\rho \equiv \rho - \rho_0$):

$$\Delta\rho S_0 + \Delta S\rho_0 = 0. \tag{5}$$

We consider a small region in a bacterial film with propagating mechanical waves that approximate plane waves. The in-plane deformation of the small region can be described by the gradients of the displacement vector field $\mathbf{d}(x,y,t)$ of mass elements in the region, with the Cartesian components of this vector field $d_1(x,y,t)$ and $d_2(x,y,t)$ representing the displacement along x and y axis.

For a mass element located at (x,y) with area S_0, when there is a displacement field $\mathbf{d}(x,y,t)$, the area of the mass element will be changed by:

$$\Delta S = S_0\left(\partial_x d_1 + \partial_y d_2\right) = S_0\nabla\cdot\mathbf{d}. \tag{6}$$

Thus, $\Delta\rho$, the cell density variation associated with the deformation of the mass element, can be written as:

$$\Delta\rho = -\frac{\rho_0}{S_0}\Delta S = -\rho_0\nabla\cdot\mathbf{d}. \tag{7}$$

In one dimension, substituting ∂_x with $-\frac{1}{v_0}\partial_t$, we have:

$$\Delta\rho = \frac{\rho_0}{v_0}\partial_t d_1. \tag{8}$$

Therefore, the cell density variation $\Delta\rho$ should be linearly proportional to the time rate of cell displacement $\partial_t d_1$, as shown in Fig. 2b (right panel).

Tension analysis. The deformation of mass elements in the quasi-two-dimensional bacterial film is determined by local tension due to pilus activities, film elasticity and substrate friction. The mechanical equilibrium satisfies:

$$0 = -\partial_i(P_0 - T) + \partial_j C_{ijkl}\partial_l d_k + \frac{f_i}{H}, \tag{9}$$

where P_0 is a constant pressure; T is the tension field (which acts isotopically and thus can be regarded as a negative pressure); C_{ijkl} is the elasticity tensor of the bacterial film; d_k ($k = 1,2$) is the k-th Cartesian component of the displacement field $\mathbf{d}(x,y,t)$; f_i is projection of friction force per unit area along the -th axis; and H is the height of bacterial

film. The magnitude of friction force per area is assumed to be constant. Choosing the x axis as the wave propagation direction, we can ignore d_2 and simplify equation (9) to:

$$\partial_x T + E\partial_x^2 d_1 + \frac{f_1}{H} = 0, \tag{10}$$

Here $E = C_{1111}$ is Young's modulus. Making use of equation (4), we can substitute all the ∂_x with $-\frac{1}{v_0}\partial_t$ and obtain the following equation:

$$0 = -\frac{1}{v_0}\partial_t T + \frac{E}{v_0^2}\partial_t^2 d_1 + \frac{f_1}{H}. \tag{11}$$

The tension T can then be solved as follows:

$$T - T_0 = \frac{C}{v_0}\partial_t d_1 + v_0\int_0^t \left(\frac{f_1}{H}\right) \mathrm{d}t', \tag{12}$$

where T_0 is a constant. Combing equations (8) and (12), we have:

$$\Delta T \equiv T - T_0 = C\frac{\Delta\rho}{\rho_0} + v_0\int_0^t \left(\frac{f_1}{H}\right) \mathrm{d}t'. \tag{13}$$

According to equation (13), the variation in tension (ΔT) is proportional to the variation in local cell density ($\Delta\rho$) plus a contribution from the friction $\int_0^t \left(\frac{f_1}{H}\right) \mathrm{d}t'$. As the friction force has a constant magnitude but its sign depends on the direction of velocity, its time integral is a periodic function having the same phase as the displacement rate $\partial_t d_1$ or local cell density $\Delta\rho$. Therefore, the tension is a periodic function in phase with local cell density; in particular, the tension at the leading side of the wavefront is expected to be higher than that at the lagging side of the wavefront, because the cell density is higher at the leading side (caption of Fig. 2a).

Non-reciprocal coupled-oscillator model

Our physical model incorporates both oscillator synchronization and continuum mechanics in the bacterial film. We modelled mass elements in the bacterial film as a system of spatially coupled phase oscillators on a two-dimensional square lattice. The phase angle of the oscillator residing in a mass element varies periodically in time while being modified by the phase angles of neighbouring oscillators within the coupling range l via non-reciprocal coupling (equation (1)). The non-reciprocal coupling is enforced by the step function $F(x)$ in equation (1). For example, consider an arbitrary pair of interacting oscillators located at positions (i,j) and (m,n), respectively. Assuming that $\theta_{(i,j)}$ lags behind $\theta_{(m,n)}$ (that is, $\theta_{(m,n)} > \theta_{(i,j)}$) without loss of generality, $\theta_{(i,j)}$ will be accelerated by ~$|\sin(\theta_{(m,n)} - \theta_{(i,j)})|\,(1+\varepsilon)/2$ and conversely, $\theta_{(m,n)}$ will be decelerated by ~$|\sin(\theta_{(i,j)} - \theta_{(m,n)})|\,(1-\varepsilon)/2$. The step function $F(x)$ ensures that the magnitude of the phase acceleration ($F > 0.5$) is higher than that of the phase deceleration ($F < 0.5$) during pairwise interactions.

In addition to the oscillator synchronization dynamics, the position of mass elements is subject to displacement due to external forces, and the displacement of mass elements may change the number of neighbours within the coupling range l for each oscillator. According to the definition of the phase angle θ of the oscillator residing in a mass element, the tension stress generated by a mass element located at (x,y) varies periodically in time and can be written as $T(x,y,t) = b(\theta)T_{\max}$, where $b(\theta) \in [0,1]$ is the duty ratio controlling the tension strength variation in the pilus retraction–extension cycle and the constant parameter $T_{\max}$ is the maximum tension stress that can be generated by a mass element in the bacterial film. The simplest form of $b(\theta)$ is $b(\theta) = \frac{\theta}{2\pi}$, so we choose $T(x,y,t) = \frac{\theta}{2\pi}T_{\max}$, where θ is in the range $[0, 2\pi]$.

While the phase angle distribution $\theta(x,y,t)$ evolves according to the non-reciprocal Kuramoto model (equation (1)), the displacement field $\mathbf{d}(x,y,t) = (d_1, d_2)$ of mass elements in the bacterial film evolves according to the following force-balance equations based on equation (9):

$$\begin{aligned} \partial_x T + E\partial_x^2 d_1 + G\partial_y^2 d_1 + f_1/H = 0, \\ \partial_y T + E\partial_y^2 d_2 + G\partial_x^2 d_2 + f_2/H = 0 \end{aligned}, \tag{14}$$

where d_1 and d_2 are the projection of the displacement field $\mathbf{d}(x,y,t)$ along x axis and y axis, respectively; E is Young's modulus; G is the shear modulus and it is related to Young's modulus in the form of $E = 2(1+\nu)G$, with ν being Poisson's ratio; f_1 and f_2 are the projection of friction force per unit area along x axis and y axis, respectively; and H is the height of bacterial film. The magnitude of friction force per area is assumed to be constant. The tension field $T(x,y,t) = \frac{\theta}{2\pi}T_{\max}$ is obtained from the time evolution of $\theta(x,y,t)$. Finally, the cell density distribution $\rho(x,y,t)$ can be obtained from the displacement field as $\rho(x,y,t) = \rho_0(1 - \nabla\cdot\mathbf{d})$, where ρ_0 is the cell density in the absence of pilus-driven tension force (equation (7)).

The simulations were performed in a 100×100 coupled-oscillator system arranged on a square-lattice domain for all results unless otherwise stated. Oscillators in the simulation domain only interacted with neighbours within the distance of coupling length; therefore, the oscillators near the boundary interacted with fewer neighbours than those inside the domain. To account for the intrinsic noise in the pilus activity of cells in the experiments, the oscillators were gradually activated (that is, being able to interact with neighbours according to equation (1)) at the beginning the simulation, with the waiting time for activating each oscillator following a normal distribution (mean, 500 time steps; standard deviation, 167 time steps). The phase angle of each oscillator at the first time step when it was activated was randomly drawn from a uniform distribution in $[0, 2\pi)$. The intrinsic angular frequency of each oscillator $\omega_{0_{(i,j)}}$ was drawn from a normal distribution (mean, $\bar{\omega}$; standard deviation, $\Delta\omega$). The Gaussian white noise $\eta(t)$ satisfies $\langle\eta(t)\eta(t')\rangle = \bar{\eta}^2\delta(t-t')$, where $\bar{\eta}$ is the noise strength. The evolution of the phase angle of each oscillator was calculated in each time step by the difference equation of equation (1):

$$\Delta\theta_{(i,j)} = \Delta t\{\omega_{0(i,j)} + \frac{\kappa}{N}\sum_{r\le l}\left[\sin\left(\theta_{(m,n)} - \theta_{(i,j)}\right)F\left(\sin\left(\theta_{(m,n)} - \theta_{(i,j)}\right)\right)\right] + \eta_{(t)}\},$$

where Δt is the time step. The tension field at the next time step was then updated as $T(t+\Delta t) = \frac{\theta(t+\Delta t)}{2\pi}T_{\max}$; with $T(t+\Delta t)$, equation (14) was solved in Fourier space to yield $\mathbf{d}(x,y,t+\Delta t)$, which was subsequently used in further evolving the phase angle distribution.

The simulation parameters used in equation (1) were chosen as follows: the intrinsic angular frequency of the oscillators $\omega_{0_{(i,j)}}$ was sampled from a Gaussian distribution with mean $\bar{\omega} = \pi/240$ rad s^{-1} and standard deviation $\Delta\omega = \pi/2{,}400$ rad s^{-1}; nearest oscillator distance d, one pixel (corresponding to 40 μm in physical space; that is mass element size being 40 μm × 40 μm); coupling length $l = 4d$, that is, four pixels or 160 μm; coupling strength κ, $\pi/80$ rad s^{-1}; time step Δt, 0.1 (for Fig. 4 and Supplementary Video 10; corresponding to 8 s in experimental time) or 0.025 (for all other simulations; corresponding to 2 s in experimental time); strength of the Gaussian white noise $\bar{\eta}$, $\pi\sqrt{\Delta t}/5$ rad s$^{\frac{-3}{2}}$ (in all simulations except for Fig. 4b;c, where $\bar{\eta}$ was set as 0 to ensure that the spiral wave pattern was stable). We found that the coupling length controls the wavelength of the resultant spiral wave pattern (estimated as ~$2\pi/|\nabla\theta(x,y,t)|$) in the simulations; the value of coupling length $l = 160$ μm was chosen so as to produce a wavelength comparable to that found in experiments. For equation (14) $T_{\max}$, the maximum tension stress (tension force per unit area) generated by a mass element in the bacterial film was estimated as $T_{\max} = (F_{\text{pilus}}/S_{\text{cell}})n_{\text{pili}}\chi = 81$ Pa; here F_{pilus} is the retraction force of one

single pilus, ~100 pN (ref. 15); $S_{cell} = [\frac{4}{3}\pi a^3 + \pi a^2 (l_B - 2a)]^{2/3}$ is the surface area of a cell, with $l_B = 3$ μm and $a = 0.4$ μm being the length and radius of a rod-shape bacterial cell, respectively; $n_{pili} = 4$ is the approximate number of type IV pili on one cell[20]; and χ is the fraction of pulus-generated tension stress that applied along an arbitrary direction, which can be calculated as: $\chi = \int_0^{\frac{\pi}{2}} \int_{-\pi}^{\pi} \sin\phi \cos\phi d\phi d\psi / \int_0^{\pi} \int_{-\pi}^{\pi} \sin\phi d\phi d\psi = 1/4$, where ϕ is the zenith angle in spherical coordinate system (assuming that bacterial pili apply isotropic retraction forces in all directions). The shear modulus $G = 40$ Pa was chosen according to our rheological measurement of artificial bacterial films (see previous section). Assuming the Poisson's ratio of the bacterial film to be 0.4, the Young's modulus E was estimated as $E = 2(1+\nu)G = 112$ Pa. The friction force per unit area f should be smaller than T_{max}, otherwise isolated cells would not be able to move on a substrate, so f was chosen to range from 1 to 10 Pa; note that f suppresses displacement but does not affect wave dynamics. Periodic boundary condition was used in the numerical simulations combining equations (1) and (14).

To study the effect of forced synchronization of oscillators in an area on the dynamics of spiral wave development (Extended Data Fig. 5 and Supplementary Video 8; that is to simulate the treatment of the artificial bacterial films with drugs that trigger pilus retraction), we forced the oscillators along one side of the boundary of the square simulation domain to synchronize their phases by manually setting the phase angle of these oscillators to be a linear function of time $\theta(t) = \omega_0 t$, where $\omega_0 = \frac{\pi}{160}$ rad s^{-1} is a constant.

To study the dynamics of spiral core interactions (Fig. 4b), the displacement of mass elements was neglected and the simulations were done with equation (1) alone with vanishing boundary condition. We artificially created two counter-rotating spiral wave patterns with opposite rotating chirality that occupied different halves of the simulation domain, by initializing the phase angle distribution of oscillators in one half as an Archimedean spiral $\theta(\rho,\phi) = \phi - \frac{\rho}{k}$ (where (ρ,ϕ) are polar coordinates and $k = 4d$ is a constant) and in the other half as the mirror-symmetric form of $\theta(\rho,\phi)$. The noise term in equation (1) was turned off and the intrinsic angular frequency of oscillators was set as a constant to exclude the effect of randomness on spiral core interactions.

To study the effect of spatial inhomogeneity or defects on a spiral wave with well-defined morphology and spiral core position (Fig. 4c and Supplementary Video 10, upper two rows), a system of 200 × 200 coupled oscillators was used; the displacement of mass elements was neglected and the simulations were done with equation (1) alone with vanishing boundary condition. We first artificially created a spiral wave with well-defined morphology and spiral core position by initializing the phase angle distribution of oscillators as an Archimedean spiral described above, with the initial spatial pattern of the wavefront (where the phase angle is zero) being $\rho = k\phi$. The system was allowed to evolve until reaching steady state, when the system displayed a stable propagating spiral wave pattern with the spiral core located at the centre of the simulation domain. Then an area with a radius of $12d$ and with its centre located at a distance $32d$ from the spiral core was chosen as the spatial defect. Oscillators in the hollow-like defect area were inactivated. The noise term in equation (1) was turned off and the intrinsic angular frequency of oscillators was set as a constant to exclude the effect of randomness on the interaction between spatial defect and existing spiral waves.

To study the effect of spatial inhomogeneity or defects on spontaneously developed spiral waves (Supplementary Video 10, lower two rows), a system of coupled oscillators was allowed to evolve spontaneously until reaching steady state, when the system displayed stable propagating spiral waves with a variable number of spiral cores in the simulation domain. Then oscillators in an area with a radius of $25d$ and located at the centre of the simulation domain were inactivated (Supplementary Video 10, lower two rows).

Data availability

The data supporting the findings of this study are included within the paper and its Supplementary Information.

Code availability

The custom codes used in this study are available from the corresponding author upon request.

References

49. Lee, K. et al. Metal-enhanced fluorescence to quantify bacterial adhesion. *Adv. Mater.* **23**, H101–H104 (2011).
50. Hentzer, M. et al. Inhibition of quorum sensing in Pseudomonas aeruginosa biofilm bacteria by a halogenated furanone compound. *Microbiology (Reading, Eng.)* **148**, 87–102 (2002).
51. Beaussart, A. et al. Nanoscale adhesion forces of Pseudomonas aeruginosa type IV pili. *ACS Nano* **8**, 10723–10733 (2014).
52. Li, Y. et al. Self-organized canals enable long range directed material transport in bacterial communities. *Elife* **11**, e79780 (2022).
53. Tremblay, J. & Déziel, E. Gene expression in Pseudomonas aeruginosa swarming motility. *BMC Genom.* **11**, 587 (2010).
54. Ma, L. Z., Wang, D., Liu, Y., Zhang, Z. & Wozniak, D. J. Regulation of biofilm exopolysaccharide biosynthesis and degradation in Pseudomonas aeruginosa. *Ann. Rev. Microbiol.* **76**, 413–433 (2022).

Acknowledgements

We thank F. Jin (Shenzhen Institute of Advanced Technology), R. Kolter (Harvard University), G. A. O'Toole (Dartmouth College) and L. Yang (Southern University of Science and Technology) for generous gifts of bacterial strains. We also thank Q. Ouyang, A. Persat, S. Strogatz, L. Tang and Z. Zheng for helpful discussions. This work was supported by the Ministry of Science and Technology Most China (No. 2021YFA0910700), the Research Grants Council of Hong Kong SAR (RGC Ref. Nos. 14307822, 14307821, RFS2021-4S04 and CUHK Direct Grants) and National Natural Science Foundation of China (NSFC No. 31971182). Y. Wu acknowledges support from New Cornerstone Science Foundation through the Xplorer Prize.

Author contributions

S.L. designed the study, performed experiments, developed the model, performed simulations, analysed and interpreted the data. Y.L. made the initial observation. Y. Wang designed the laser ablation setup. Y. Wu conceived the project, designed the study and analysed and interpreted the data. Y. Wu wrote the paper with S.L.'s input.

Competing interests

The authors declare no competing interests.

Additional information

Extended data is available for this paper at https://doi.org/10.1038/s41567-024-02457-5.

Supplementary information The online version contains supplementary material available at https://doi.org/10.1038/s41567-024-02457-5.

Correspondence and requests for materials should be addressed to Yilin Wu.

Peer review information *Nature Physics* thanks David Johnson and Michael Shelley for their contribution to the peer review of this work.

https://doi.org/10.1038/s41567-024-02457-5

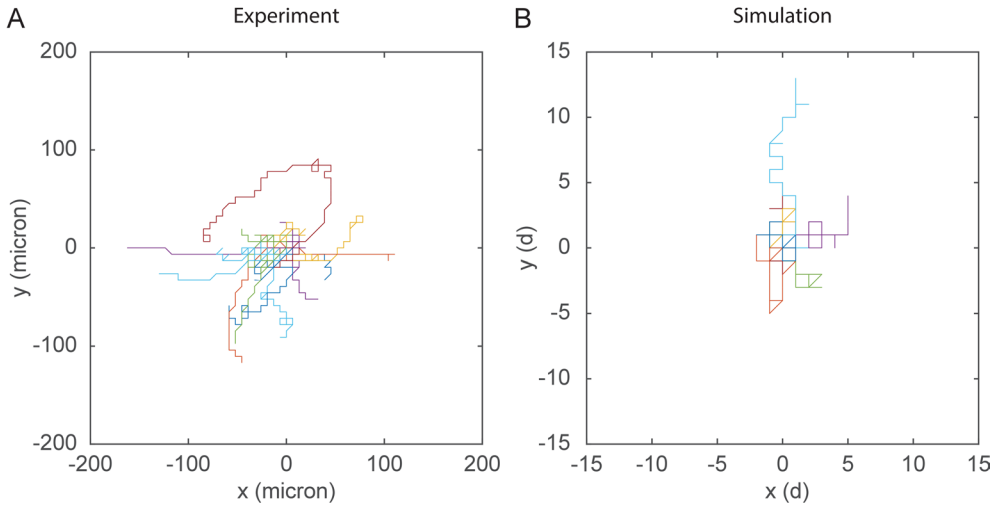

Extended Data Fig. 1 | Trajectories of spiral cores of propagating spiral waves at steady state. (**a**) Representative spiral core trajectories acquired experimentally in artificial bacterial films of piliated *P. aeruginosa* (PA14 *flgK*::Tn5). Each trajectory lasted for ~1 hour. The range of spiral core motion is a few tens of μm and two order of magnitude smaller than the wavelength (~1 mm). The trajectories appeared random and showed no periodic meandering motion. The trajectories of different cores are labelled with different colour. The initial position of each core is set to x = 0, y = 0 for better comparison. (**b**) Representative spiral core trajectories in numerical simulations of the nonreciprocal coupled oscillator model with a full nonreciprocity ($\varepsilon = 1$) associated with main text Fig. 3f. The trajectories are plotted in the same manner as in panel A.

https://doi.org/10.1038/s41567-024-02457-5

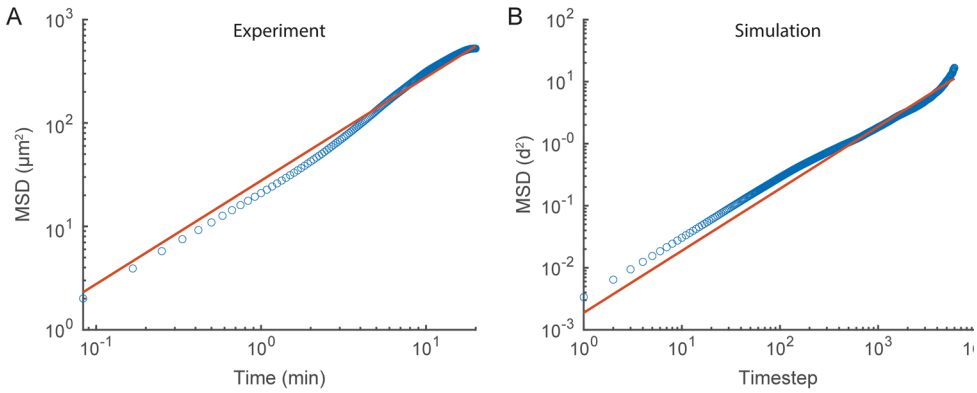

Extended Data Fig. 2 | Mean-square displacement (MSD) and diffusivity of spiral cores measured in experiments (panel A; with 20 spiral cores) and in simulations (panel B; with 15 spiral cores). Blue circles: MSD data. Red line: MSD fitted to $4Dt$, with D being the diffusion coefficient. The collective MSD of all spiral cores was computed by segmenting spiral core trajectories with different time windows. Note that the trajectories of spiral cores obtained in experiments were corrected for their own drift, which was likely caused by cell growth during the tracking period; for the -th core, its drift (denoted as v_d) was computed by fitting the core's own MSD (denoted as MSD_i) to $at + (v_d t)^2$, and its drift-corrected MSD is calculated as $\overline{MSD_i} = MSD_i - (v_d t)^2$. Then the overall drift-corrected MSD of N spiral cores, defined as $MSD_{all} = \sum \overline{MSD_i}/N$, was fitted to $MSD_{all} = 4Dt$ as shown in panel A. In panel A, $D = 6.92\mu m^2/min$ (equivalent to 4.80×10^{-5} square wavelengths per period). In panel B, $D = 9.72 \times 10^{1}\ \mu m^2/min$ (equivalent to 6.14×10^{-4} square wavelengths per period).

https://doi.org/10.1038/s41567-024-02457-5

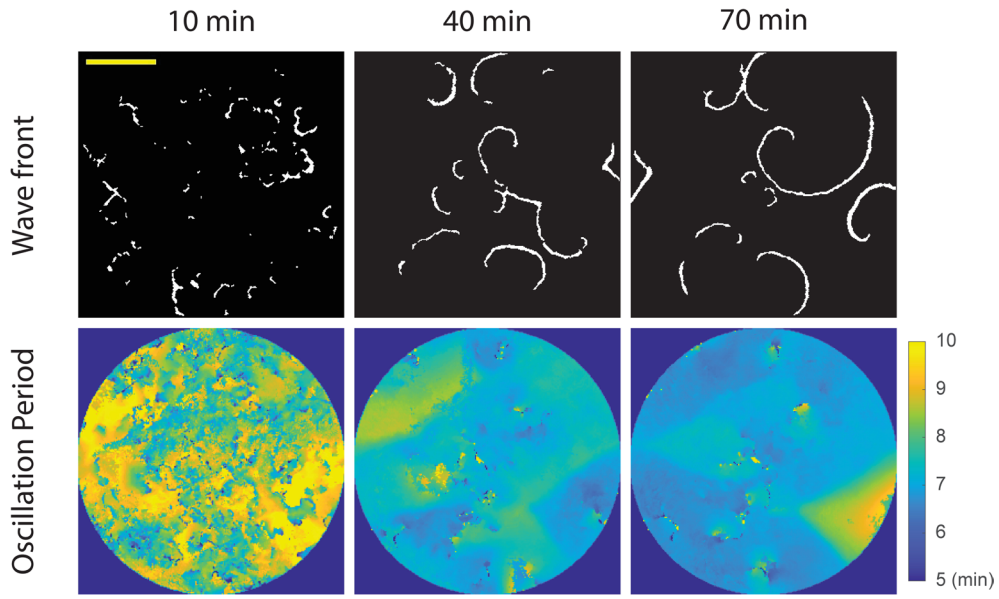

Extended Data Fig. 3 | Development of propagating spiral waves in disk-shaped artificial bacterial films of *P. aeruginosa*. Upper row: Traces of wavefronts (identical to upper row of main text Fig. 1c). Lower row: Distributions of local instantaneous oscillation period during the spiral wave development (Methods). Color bar to the right of the lower row indicates the magnitude of instantaneous oscillation period (unit: min). Scale bar, 500 μm. Also see Movie 2.

https://doi.org/10.1038/s41567-024-02457-5

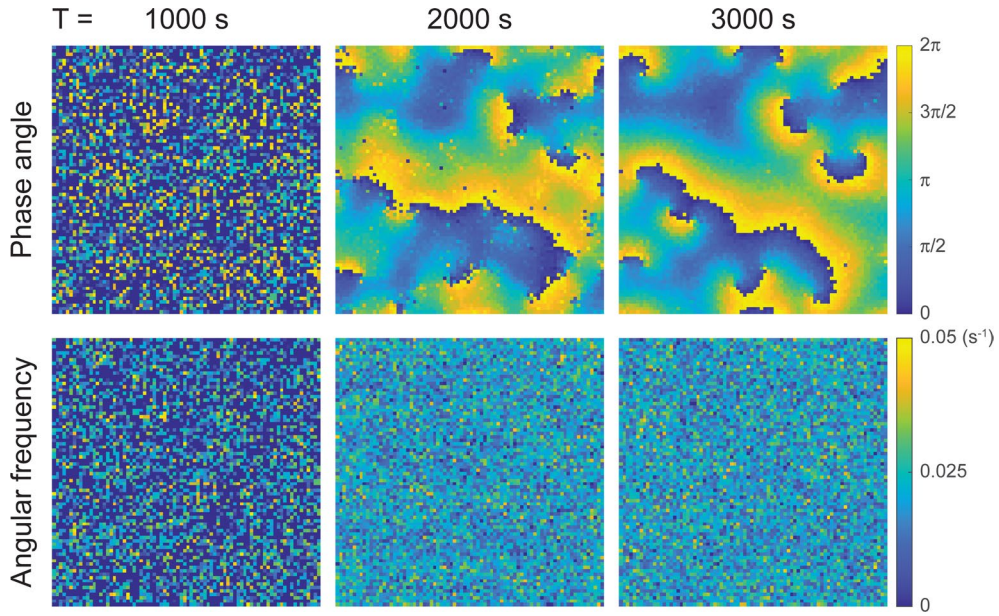

Extended Data Fig. 4 | Spatiotemporal dynamics of phase angle (upper) and angular frequency distribution (lower) in simulations of the nonreciprocal coupled oscillator model with a full nonreciprocity ε = 1. Upper row: Phase angle distribution (identical to main text Fig. 3b). Lower row: Distributions of local instantaneous angular frequency during the spiral wave development (Methods). Color bar to the right of the lower row indicates the magnitude of instantaneous oscillation angular frequency. Also see Movie 7.

https://doi.org/10.1038/s41567-024-02457-5

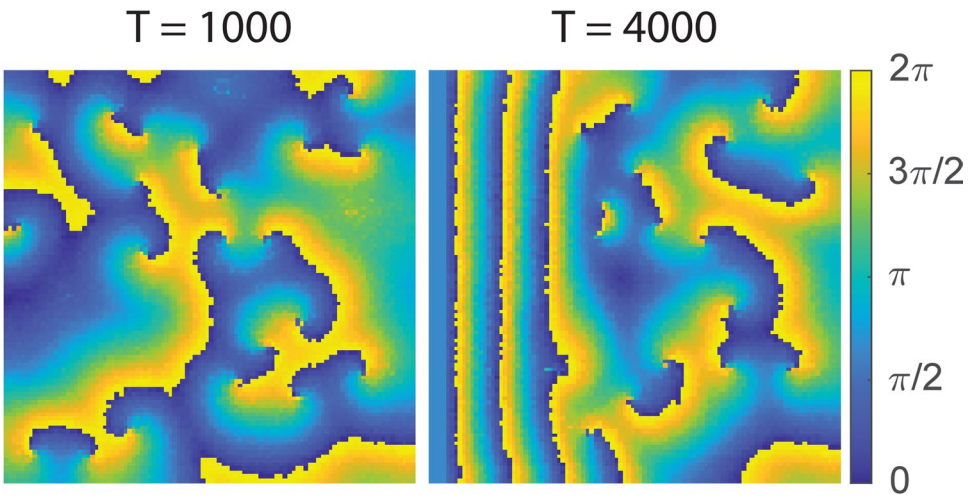

Extended Data Fig. 5 | Generation of train waves by forced synchronization of oscillators in the nonreciprocal coupled oscillator model with a full nonreciprocity $\varepsilon = 1$. The simulation was performed in a system with pre-existing propagating spiral waves (left panel, T = 2400 s). Starting from T = 2408 s, the oscillators near the left boundary were forced to synchronize and remained synchronized throughout the rest of the simulation, which simulated the application of a filter disk infused with drugs that trigger pilus retraction. Following the forced synchronization, train waves emanated from near the left boundary and propagated along a direction perpendicular to the boundary (right panel, T = 4000 s and T = 16000 s). The train waves gradually replaced the existing spiral waves. Also see Methods and Movie 8. The results reproduce the experimental phenomena in Movie 5 and Movie 6, supporting the notion that train waves observed in the experiments were due to forced synchronization of the pilus retraction-extension cycle.